Supplementary Information

Atomic-layer-resolved composition and electronic structure of the cuprate $Bi_2Sr_2CaCu_2O_{8+\delta}$ from soft x-ray standing-wave photoemission

Cheng-Tai Kuo[1,2*], Shih Chieh Lin[1,2], Giuseppina Conti[1,2], Shu-Ting Pi[1], Luca Moreschini[3], Aaron Bostwick[3], Julia Meyer-Ilse[2], Eric Gullikson[2], Jeffrey B. Kortright[2], Slavomir Nemšák[4], Julien E. Rault[5], Patrick Le Fèvre[5], François Bertran[5], Andrés F. Santander-Syro[6], Ivan A.Vartanyants[7,8], Warren E. Pickett[1], Romuald Saint-Martin[9], Amina Taleb-Ibrahimi[5], Charles S. Fadley[1,2]

Affiliations

[1]Department of Physics, University of California Davis, Davis, California 95616, USA

[2]Materials Sciences Division, Lawrence Berkeley National Laboratory, Berkeley, California 94720, USA

[3]Advanced Light Source, Lawrence Berkeley National Laboratory, Berkeley, California 94720, USA

[4]Peter Grünberg Institut PGI-6, Research Center Jülich, 52425 Jülich, Germany

[5]Synchrotron SOLEIL, L'Orme des Merisiers, Saint-Aubin-BP48, 91192 Gif-sur-Yvette, France

[6]CSNSM, Université Paris-Sud, CNRS/IN2P3, Université Paris-Saclay, 91405 Orsay Cedex, France

[7]Deutsches Elektronen-Synchrotron DESY, Notkestraße 85, D-22607 Hamburg, Germany

[8]National Research Nuclear University MEPhI (Moscow Engineering Physics Institute), Kashirskoe Shosse 31, Moscow, 115409, Russia

[9] SP2M-ICMMO-UMR-CNRS 8182, Université Paris-Sud, Université Paris-Saclay, 91405 Orsay Cedex, France

*E-mail:chengtaikuo@lbl.gov

S1. Sample preparation and characterization

$Bi_2Sr_2CaCu_2O_{8+\delta}$ (Bi2212) single crystal growth was performed in an optical floating zone furnace (Crystal System Incorporation, Japan) equipped with four 300W lamps installed as infrared radiation sources. The sintered feed rods used for the crystal growth, prepared by the conventional solid-state reaction, were pre-melted in air with a mirror scanning velocity of 15mm/h by traveling the upper and lower shaft to densify the feed rod and to avoid the emergence of bubbles during the crystal growth. A previously grown Bi2212 crystal ingot was used as a seed rod. The feed rod and the growing crystal were rotated at 15 rpm and 20 rpm, respectively, in opposite directions to ensure efficient mixing and uniform temperature distribution in the molten zone. Different growth rates (0.5 to 2.5 mm/h) and atmosphere pressure (1, 2 and 3 bars) were applied but the highest-quality single crystals were obtained for a slow growth rate of 0.6mm/h and an oxygen pressure $p(O_2)$ = 2 bar. X-ray diffraction measurements were performed in order to rule-out the possible presence of a secondary phase. The critical temperature, which is determined from the onset of the SQUID diamagnetic transition, is ~93K.

Before the photoemission measurements, the Bi2212 single crystal was cooled down to ~77K by liquid N_2 below its superconducting transition temperature and *in situ* cleaved in the analysis chamber. Angle-resolved photoemission spectroscopy (ARPES) at hv = 110 eV was used for initial sample alignment. Figure S1a shows the Fermi surface of Bi2212 measured by ARPES at 110 eV and it shows the typical patterns as the prior studies[1,2]. The measurement was performed to confirm a well-ordered region of the cleaved surface by scanning in x and y and to precisely align the crystal to the Bragg reflection condition; this was repeated after our standing-wave excited photoemission (SW-XPS) measurements to verify surface stability. The SW-XPS was measured at 930.3 eV, for which we were unable to observe any momentum resolution, likely due to some combination of the supermodulation in the crystal and the momentum-smearing effects of phonons. The details of choosing a suitable SW excitation energy are discussed in the next section. The beam size was 100 μm x 200 μm. The binding energy was calibrated using a gold reference sample. The estimated experimental resolution for the SW measurements is 0.6 eV. A survey spectrum (Fig. S1b) of the cleaved Bi2212 surface

shows core levels from all the expected elements present, with no indication of a surface contaminant signal from C 1s; surveys before and after our measurements yielded the same conclusion.

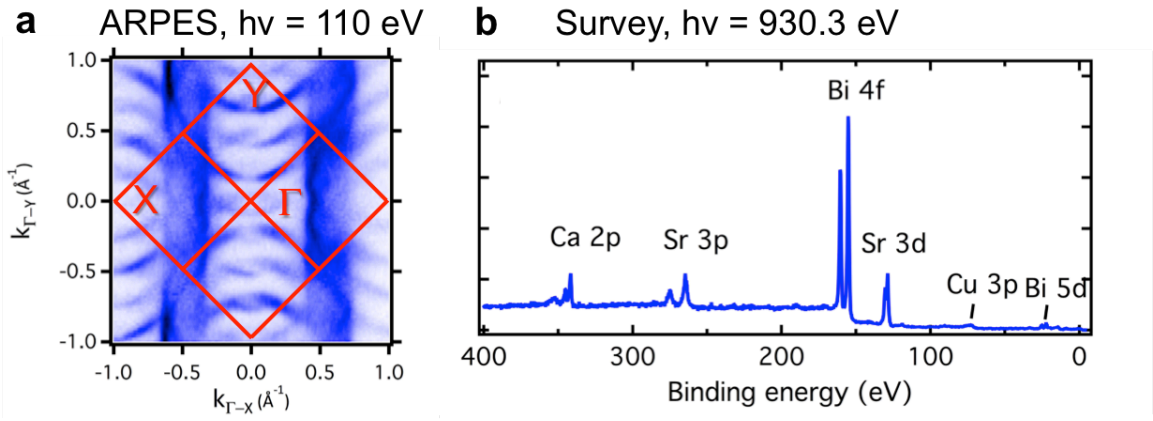

Figure S1 Photoemission characterization of cleaved Bi2212. a, ARPES Fermi surface obtained at hv = 110 eV, and **b**, a survey spectrum obtained at our SW energy of hv =930.3 eV.

S2. Cu L_3 edge resonant effect on absorption, reflectivity and SW strength

The strength of the SW is proportional to the square root of the reflectivity, R, with overall amplitude of modulation of ~2(R)$^{1/2}$ according to SW theory based on dynamical x-ray diffraction[3,4,5]. In order to maximize the reflectivity, and thus the SW effect, the excitation energy was varied through the strong Cu L_3 edge (Fig. S2a), as demonstrated recently for a multilayer oxide heterostructures[6]. Reflectivity was measured at Beamline 6.3.2 of the Advanced Light Source. Figure 2b plots the reflectivity as a function of the excitation energy (blue curve), and it shows that the maximum of reflectivity is at 930.3 eV, which is ~1.6 eV below the L_3 x-ray absorption (XAS) peak (black curve), also shown in this panel. The reflectivity for two energies near the resonance (cuts A and B in Fig. S2a) has also been analyzed using SW theory (green and red curves in Fig. S2c), and they exhibit excellent agreement with experiment (green and red dots in Fig. S2c), including the marked increase in reflectivity on going just below the absorption

maximum (cf. also Fig. S2b). The angular scan of reflectivity at 930.3 eV (cut A in Figs. S2a,c) has a maximum of ~2.6x10^{-4}, leading to a maximum of standing wave modulation of ~ $2\sqrt{R}$ ~ 3% (see further details for SW modeling below). Note that the RC modulations in Figs. 2e-i in the article are in the 5-10% range, roughly consistent with this estimate, especially since we could not cleave the sample surface for the reflectivity measurement. For comparison, the maximum of reflectivity at the XAS peak (cut B in Figs. S2a,c) shows a decrease to ~1x10^{-4} that would reduce the SW modulation by about one half. Therefore, all our SW-XPS measurements were carried out at hv = 930.3 eV.

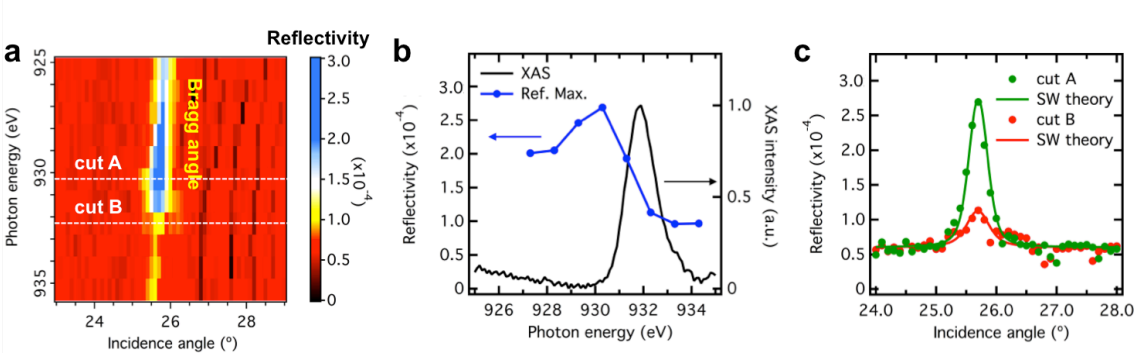

Figure S2 Resonant effects on the (002) Bragg reflection in Bi2212 near the Cu L_3 edge. a, Reflectivity as a function of incidence angle and photon energy near the Cu L_3 edge. **b**, Comparison of the maximum reflectivity (Ref. Max., left axis, blue line) as a function of photon energy and the x-ray absorption spectrum (XAS, right axis, black line). **c**. Reflectivity as a function of angle for two photon energies (cuts A and B in **a**. The points are angular scans of reflectivity measured around the Bragg angle at hv = 930.3 (cut A in **a**) and 932.3 eV (cut B in **a**). The experimental data (points) are compared with the SW theory (curves).

S3. Core-level rocking curves: SW modeling based on dynamical diffraction

The normalized core-level rocking curves (RCs) in Figs. 2,3 of the main text have been analyzed using SW theory based on dynamical x-ray diffraction, as applied in particular to photoemission[3,4,5]. The SW intensity for a given H = (*hkl*) reflection of a given element Q from a given depth z_i below the surface is

$$I_{SW,HQ}(z_i,\theta_{inc}) = I_0 \exp^{-\frac{z_i}{\Lambda_x^{eff}\sin\theta_{inc}}}\left[1+R(\theta_{inc})+2C\sqrt{R(\theta_{inc})}f_{HQ}\cos(\varphi_H(\theta_{inc})-2\pi P_{HQ}(z_i))\right], \quad \text{(S1)}$$

where I_0 is the incident intensity, Λ_x^{eff} is the effective attenuation length of x-ray due to both absorption and diffraction, R is the reflectivity at a given incidence angle θ_{inc}, measured with respect to the surface, C=2cos(2θ_B) is the polarization factor for π-polarization, θ_B is the Bragg angle for the H reflection, f_{HQ} is the coherent fraction of atoms of type Q for the H reflection, φ_H is the phase difference between the incident and diffracted waves, and P_{HQ} is the coherent position of atom Q for the H reflection at depth z_i. For our Bi2212 sample, direct calculations reveal that the absorption length is ~75 nm and the extinction length due to diffraction is 1775 nm; thus Λ_x^{eff} ≈71 nm is much greater than the inelastic mean free path for electrons, which is ~1-1.5 nm, and so we can set the exponential to unity in Eq. (S1).

An effectively angle-integrated photoemission intensity for a give H reflection, emission from the nℓ level of a given element Q, which is the core-level RC, can then be calculated as

$$I_{Qn\ell}(\theta_{inc}) = \rho_Q \frac{d\sigma_{Qn\ell}}{d\Omega}\left[1+R(\theta_{inc})+\sum_i^N \frac{e^{\frac{-z_i}{\Lambda_e\sin\theta_e}}}{I_A}\times 2\cos(2\theta_B)\sqrt{R(\theta_{inc})}f_{HQ}\cos(\varphi_H(\theta_{inc})-2\pi P_{HQ}(z_i))\right], \quad \text{(S2)}$$

where ρ_Q is the density of atom Q and $d\sigma_{Qn\ell}/d\Omega$ is the differential photoelectric cross section of level $Qn\ell$. The exponential allows for photoelectron attenuation due to inelastic scattering, where Λ_e is the electron inelastic mean-free paths and θ_e is the electron emission angle with respect to the sample surface. I_A is a normalization factor for photoelectron intensities that represents the sum over all layers in the absence of the SW effect: $I_A = \sum_j^N e^{\frac{-z_j}{\Lambda_e\sin\theta_e}}$. In each core-level RC, the intensity is finally normalized to 1 at off-Bragg position as the atom density and differential don't affect its phase and modulation of intensity, thus providing an element-specific measure of the fractional modulation due to the SW at a given atomic type.

Figure S3 shows the geometry of our SW measurement, and illustrates the definition of incidence and emission angles: e.g., for our geometry, $\theta_e = \theta_{inc} + 54°$. $Qn\ell$ for our case thus involves layers containing Cu 3p, Sr 3d, Bi $4f_{7/2}$, two types of Ca 2p, and three of O 1s (denoted P1, P2, and P3 in the text). In Eq. (S2) the summation was taken with N over 3 unit cells, which translates through the electron inelastic mean free path to including 99.6% of the photoelectron intensity. The photoelectrons were collected in a partially angle-integrated manner, as the analyzer collected photoelectrons from the +/- 6 degrees of the analyzer lens axis, and emission was near the (001) sample normal.

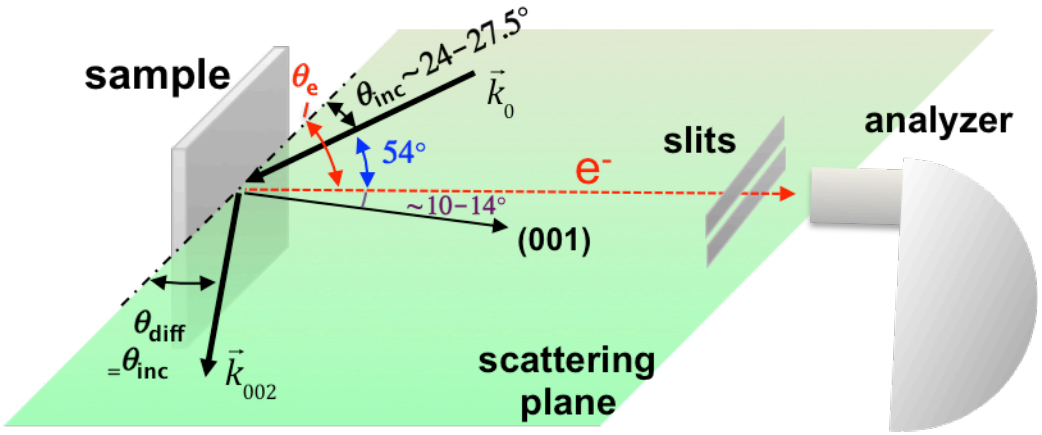

Figure S3 Geometry of SW-XPS measurement. The incidence angle between the incident light with wave vector and the sample surface varies from 24 to 27.5°. The experimental geometry fixes the angle between the incident light and the outgoing photoelectrons at 54°.

The reflectivity, $R(\theta_{inc})$ and phase $\varphi_H(\theta_{inc})$, including dynamical diffraction effects, were calculated from Eq. (S3) (Ref. 3), which contains three fitting parameters in the factors at right:

$$R(\theta_{inc}) = \left|\frac{E_H}{E_0}\right|^2 = \left|\eta \pm (\eta^2 - 1)^{\frac{1}{2}}\right|^2 \left|\frac{F_H}{F_{\bar{H}}}\right|^2 \times \frac{1}{\sigma\sqrt{2\pi}} e^{\frac{-\Delta\theta^2}{2\sigma^2}} \times e^{-W}. \quad \text{(S3)}$$

Here, E_H and E_0 are the complex electric field amplitudes of the incident and diffracted waves, with H = (002) reflection, η is defined below and is a normalized angle parameter

dependent on the deviation of the angle θ_{inc} from the Bragg angle θ_B, F_H and $F_{\bar{H}}$ are the structure factors for H and $\bar{H}$ reflections, σ is the Gaussian width of the reflectivity curve, incorporating e.g. the x-ray beam divergence, and W is the Debye-Waller factor = $\exp(-H^2\langle u^2\rangle/3)$, where H is the scattering vector, and $\langle u^2\rangle$ is the mean-square atomic displacement. Thus, σ determines the width of the reflectivity curve and the RCs, and W determines the intensity of reflectivity and the RC modulation. The first factor before the multiplication sign in $R(\theta_{inc})$ is the reflectivity from an ideal crystal. The next factor allows for mosaicity in the crystal and x-ray beam divergence and the fourth factor for vibrational motion and static distortions of atomic positions from the ideal structure, as e.g. the supermodulation of atomic positions in the crystal structure. The normalized angle parameter η is defined as:

$$\eta = \frac{-\Delta\theta \sin 2\theta_B + \frac{r_e\lambda_x^2}{\pi V}F_0}{\frac{r_e\lambda_x^2}{\pi V}\sqrt{F_H F_{\bar{H}}}}, \qquad \text{(S4)}$$

where $\Delta\theta = \theta_{inc} - \theta_B$, r_e is the classical electron radius, λ_x is the wavelength of the x-ray, V is the total volume of the unit cell, and F_0 is the structure factor for (000) reflection.

The σ and W values determined from a combined analysis of the reflectivity and SW photoemission data are 0.28±0.02° and 2.95±0.04, with the large value for the second factor probably being due to the supermodulation and residual surface roughness after the cleave. After fitting all of the core-level RCs, we derive f_{HQ} and P_{HQ} values, as well as the absolute positions (z_Q) of the first contributing layers, and these are shown in Supplementary Table S1. These numbers confirm our assignment of Ca(HBE) to the SrO layer, a displacement of the O atoms from the Cu atoms in the CuO layer, and a displacement of the O atoms in the Sr layer, as discussed in the main text. These displacements are consistent with prior transmission electron microscopy and x-ray diffraction results for Bi2212[7,8]. The quantity f_{HQ} determines the amplitude of RCs and indicates the width of the absolute position distribution, where by definition f_{HQ} = 1 means diffraction from perfectly flat layers. P_{HQ} determines the shape of RCs and provides the average atomic positions (z_Q). The values of f_{HQ} are generally low in Bi2212,

which is related to the atomic displacements or supermodulation structure in Bi2212. The very low value of f_{HQ} for O in the CuO layer might be related to more vibrational disorder and the presence of supermodulation.

Supplementary Table S1 The values of f_{HQ}, P_{HQ}, and the absolute positions (z_Q) of the first contributing planes in the unit cell, as determined by fitting the core-level RCs to Eq. (S2). The *c* lattice constant of Bi2212 is 30.7 Å[7]. Estimated errors are: $\Delta f_{HQ} = \pm 0.03$, $\Delta P_{HQ} = \pm 0.02$, $\Delta z_Q = d_{002} \times \Delta P_{HQ} = \pm 0.31$ Å.

Atom	f_{HQ}	P_{HQ}	z_Q (Å)	Atom	f_{HQ}	P_{HQ}	z_Q (Å)
Bi	0.55	0.92	29.47	Cu	0.58	0.53	23.49
O(Bi)	0.45	0.92	29.47	O(Cu)	0.21	0.60	24.56
Ca(LBE)	0.54	0.50	23.03	Sr	0.36	0.67	25.63
Ca(HBE)	0.41	0.67	25.63	O(Sr)	0.43	0.77	27.17

S4. Valence-band rocking curves: SW modeling based on dynamical diffraction

In analyzing the valence-band RC of Fig. 4a in the main text, we have made the assumption that the matrix elements are primarily controlled by the region near the core, as discussed previously in connection with XPS or HAXPES spectra[4,5,9,10,11]. The intensity from a given valence subshell $Qn\ell$ in layer *i* at depth z_i can then, by analogy with Eq. (S2) be described by

$$I_{VB,Qn\ell,i}(E_b,\theta_{inc}) = \rho_{Qn\ell,i}(E_b)\frac{d\sigma_{Qn\ell}}{d\Omega}\left[1+R(\theta_{inc})+\sum_i^N \frac{e^{\frac{-z_i}{\Lambda_e \sin\theta_e}}}{I_A}\times 2\cos(2\theta_B)\sqrt{R(\theta_{inc})}f_{HQ}\cos(\varphi_H(\theta_{inc})-2\pi P_{HQ}(z_i))\right], \quad \text{(S5)}$$

where $\rho_{Qnl,k}(E_b)$ is the density of states in layer *i*, projected onto $Qn\ell$ character, but assumed not to change with layer, so the *i* index can be dropped to $\rho_{Qnl}(E_b)$, $d\sigma_{Qnl}(h\nu,\varepsilon)/d\Omega$ is the energy- and polarization- dependent differential photoelectric cross section for subshell $Qn\ell$. The total valence band intensity is thus

$$I_{VB}(E_b,\theta_{inc}) = \sum_{Qn\ell,i} I_{VB,Qn\ell}(E_b,\theta_{inc}) = \sum_{Qn\ell,i} \rho_{Qn\ell}(E_b)\frac{d\sigma_{Qn\ell}}{d\Omega} I_{Qn\ell,i}(\theta_{inc}) \equiv \sum_{Qn\ell,i} D_{Qn\ell}(E_b) I_{Qn\ell,i}(\theta_{inc}), \quad \text{(S6)}$$

where we have defined

$$D_{Qn\ell}(E_b) = \rho_{Qn\ell}(E_b)\frac{d\sigma_{Qn\ell}}{d\Omega}, \quad \text{(S7)}$$

which will be the experimentally layer-projected quantity; see Eq. (1) in the main text. Now, assuming that the normalized SW effect on a core-level $Qn'\ell'$ in the same layer is the same as that for the $Qn\ell$ valence level, we have from Eqs. (S6) and (S7):

$$I_{VB}(E_b,\theta_{inc}) = \sum_{Qn\ell} I_{VB,Qn\ell}(E_b,\theta_{inc}) = \sum_{Qn\ell} D_{Qn\ell}(E_b)\overline{I}_{Qn'\ell'}(E_b), \quad \text{(S8)}$$

which is equivalent to Eq. (1) in the main article. The $Qn\ell$ choices for us are those for which the cross sections are dominant, as described in the text: *Cu 3d* in CuO_2, *Sr 4p* in SrO, and *Bi 5d* in BiO, which makes the rocking curves for *Cu 2p, Sr 3d* and *Bi* $4f_{7/2}$ the natural choices for the $\overline{I}_{Qn'\ell'}(\theta_{inc})$ in our analysis.

S5. Photoelectric cross-section-weighted DOSs

As mentioned in the test and the previous section, a given valence spectrum is a linear sum of the individual DOSs $\rho_{Qn\ell}(E_b)$ weighted by matrix elements, or in our assumed high-energy limit, the differential photoelectric cross section $d\sigma_{Qn\ell}/d\Omega$. The differential photoelectric cross section, using the dipole approximation, is given by equation (S9)[12]:

$$\frac{d\sigma_{Qn\ell}(h\nu,\varepsilon)}{d\Omega}=\frac{\sigma_{Qn\ell}}{4\pi}[1+\frac{\beta}{2}\left(3\cos^2\alpha-1\right)], \tag{S9}$$

where $\sigma_{Qn\ell}$ is the total photoionization cross section of subshell $Qn\ell$, β is the dipole asymmetry parameter, α is the angle between the direction of photoelectron emission and the polarization direction. The experimentally layer-projected DOS $D_i(E_b)$ from the three characteristic atom layers (i = BiO, SrO, and CuO_2) approximately equals the cross-section-weighted DOSs summed over the constituting atoms in the same layer. For example, the layer-projected CuO_2 DOS is

$$D_{\mathrm{CuO_2}}(E_b)\approx\sum_{Cu-n\ell}\frac{d\sigma_{Cu-n\ell}}{d\Omega}\rho_{Cu-n\ell}(E_b)+\sum_{O-n\ell}\frac{d\sigma_{O-n\ell}}{d\Omega}\rho_{O-n\ell}(E_b). \tag{S10}$$

Supplementary Table S2 lists the cross sections and asymmetry parameters of the dominant atomic orbitals in VB intensity for the elements in Bi2212, which are used for calculating the cross-section-weighted DOSs of BiO, SrO, and CuO_2 layers. The values were obtained from Ref. 13. The fact that the angle between incidence and polarization is very near the magic-angle for which $3\cos^2\alpha-1$ is zero means that the asymmetry parameter has little influence. Figure S4a shows the layer-projected DOSs from each layer calculated by DFT calculations incorporating the known supermodulation structures. Their resulting cross-section-weighted DOSs are shown in Fig. S4b, which are also presented in Figs. 4c,d of the article.

Supplementary Table S2 The cross sections (σ_{nl}) and asymmetry parameters (β) of the dominant atomic orbitals in VB intensity for all the elements in Bi2212.

Element	Orbital	σ_{nl}	β	Element	Orbital	σ_{nl}	β
Ca	4s	0.0010	2.00	O	2s	0.0067	2.00
	3p	0.0251	1.45		2p	0.0014	0.70
Cu	4s	0.0007	2.00	Bi	6s	0.0030	2.00
	3p	0.1003	1.60		6p	0.0028	1.67
	3d	0.0422	1.11		5d	0.0919	1.21
Sr	5s	0.0008	2.00				
	4p	0.0271	1.67				

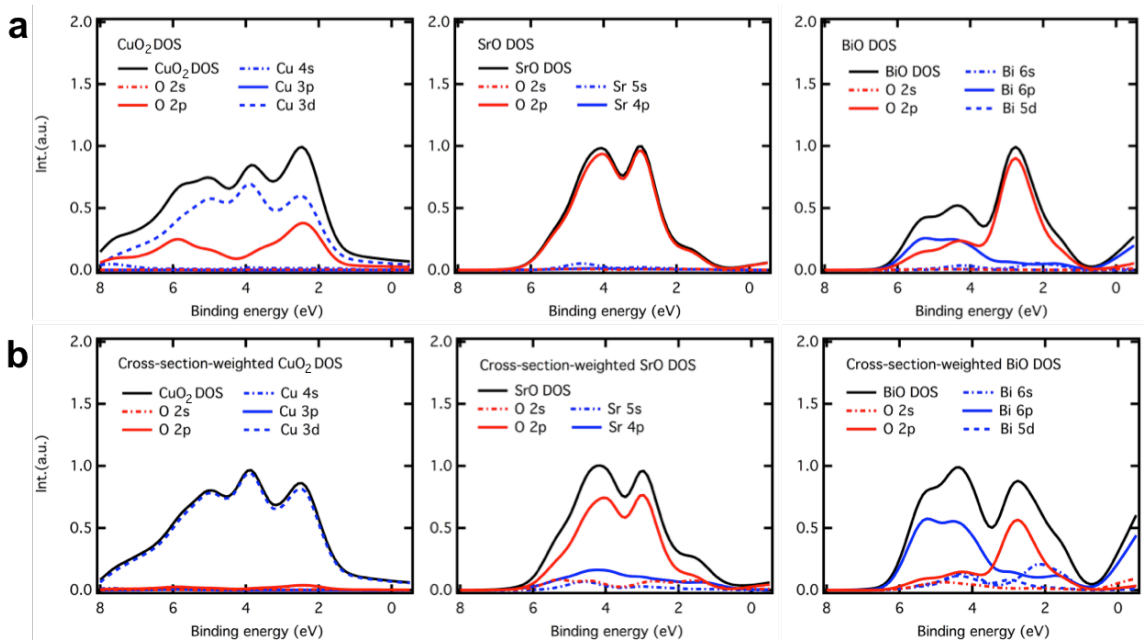

Figure S4 Photoelectron-cross-section-weighted DOSs. a, The layer-projected DOSs calculated by DFT calculations incorporating the known supermodulation structures. **b**, The resulting layer-projected, cross-section-weighted DOSs calculated using equations (S9) and (S10).

S6. Atomic coordinates and density functional theory calculations

The atomic coordinates and lattice constants of Bi2212 with and without supermodulation (SM) structure used for our DFT calculations and for our SW dynamical diffraction calculations are listed in Supplementary Table S3 and Table S4, respectively. The unit cell of Bi2212 with supermodulation (SM) structure is $\sqrt{2}a \times \sqrt{2}a \times c$, but the unit cell of Bi2212 without SM is $a \times a \times c$. Therefore, the larger in-plane lattice constants for the Bi2212 with SM leads to a smaller 1st Brillouin zone. The bands of Bi2212 without SM structure are folded in order to directly compare their band structures at the high symmetry points, as shown in Fig. S5.

Supplementary Table S3 The structural properties, such as the atomic coordinates and lattice constants, of ideal Bi2212 for DFT calculations. The space group is I4/mmm and the lattice constants a = b = 3.825 Å, c = 30.82 Å. These values are obtained from Ref. 14. x, y, and z are expressed as fractions of a, b, and c. For these coordinates, the center of the unit cell is in the Ca layer.

Element	Multiplicity	x	y	z
Bi	4	0	0	0.3
Sr	4	0	0	0.1
Cu	4	0.5	0.5	0.05
Ca	2	0	0	0
O(1)	8	0	0.5	0.05
O(2)	4	0	0	0.2
O(3)	4	0	0	0.385

Supplementary Table S4 The structural properties, such as the atomic coordinates and lattice constants, of supermodulated Bi2212 for DFT calculations. The space group is Amaa (No. 66), and the lattice constant a = 5.4054 Å, b = 5.4016 Å, c = 30.7152 Å. These values are obtained from Ref. 7. x, y, and z are expressed as fractions of a, b, and c. For these coordinates, the center of the unit cell is in between the Bi atoms.

Element	Multiplicity	x	y	z
Bi	8	0.052	0.2745	0.0524
Sr	8	0	0.75	0.3597
Cu	8	0.5	0.75	0.3033
Ca	4	0.5	0.25	0.25
O(1)	8	0.75	0	0.201
O(2)	8	0.25	0.5	0.201
O(3)	8	0	0.25	0.385
O(4)	8	0.5	0.27	0.0524

We note here that it has also been observed that the SM structure can in fact have a larger period, including up to a fivefold larger unit cell in plane[15,16]. We have here only considered the SM in a twofold enlargement of the unit cell, due to the much greater computational effort required to include SM up to the fivefold larger in-plane unit cell, and we believe this should include most of the essential physics.

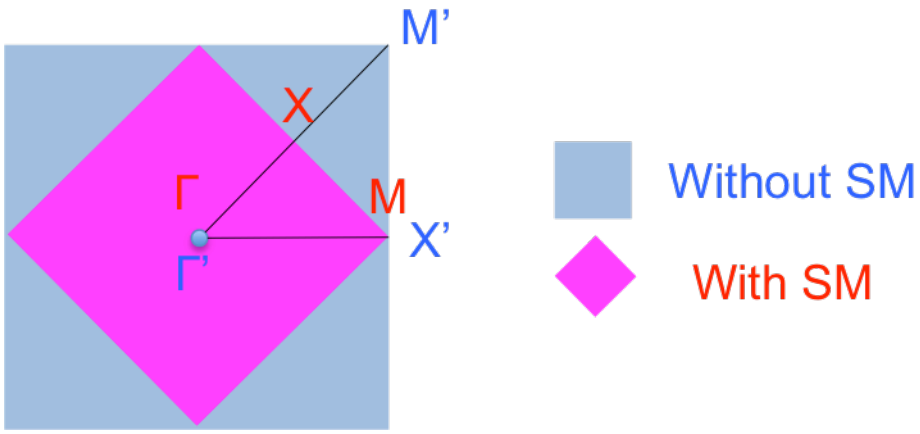

Figure S5 1st Brillouin zone of the Bi2212 with and without supermodulation (SM) structure. M', X', and Γ' are the high symmetry points for Bi2212 without SM, while M, X, and Γ are for Bi2212 with SM.

[1] Aebi, P. *et al.* Complete Fermi surface mapping of $Bi_2Sr_2CaCu_2O_{8+x}$(001): Coexistence of short range antiferromagnetic correlations and metallicity in the same phase. *Phys. Rev. Lett.* **72**, 2757 (1994).
[2] Damascelli, A., *et al.* Angle-resolved photoemission studies of the cuprate superconductors. *Rev. Mod. Phys.* **75**, 473-541 (2003).
[3] Batterman, B. W. and Cole, H. Dynamical diffraction of x rays by perfect crystals. *Rev. Mod. Phys.* **36**, 681-717 (1964).
[4] Woicik, J. C. *et al.* Partial density of occupied valence states by x-ray standing waves and high-resolution photoelectron spectroscopy. *Phys. Rev. B* **63**, 041403R (2001).
[5] Vartanyants, I. A. and Kovalchuk, M. V. Theory and applications of x-ray standing waves in real crystals. Rep. Prog. Phys. 64, 1009-1084 (2001).
[6] Gray, A.X., *et al.* Interface properties of magnetic tunnel junction $La_{0.7}Sr_{0.3}MnO_3/SrTiO_3$ superlattices studied by standing-wave excited photoemission spectroscopy. *Phys. Rev. B* **82**, 205116 (2010).
[7] Hervieu, M. *et al.* Electron microscopy study of the superconductor "$Bi_2Sr_2CaCu_2O_{8+\delta}$". *Mod. Phys. Lett. B* **2**, 491-500 (1988).
[8] Sunshine, S. A. *et al.* Structure and physical properties of single crystals of the 84-k superconductor $Bi_{2.2}Sr_2Ca_{0.8}Cu_2O_{8+\delta}$. *Phys. Rev. B* **38**, 893-896 (1988).
[9] Gelius, U. in *Electron Spectroscopy*, Shirley, D. A. Ed. (North Holland, 1971) p. 311
[10] Solterbeck, C. *et al.* Energetic and spatial bonding properties from angular distributiona of ultraviolet photoelectrons: Applications to the GaAa(110) surface. *Phys. Rev. Lett.* **79**, 4681-4684 (1997).
[11] Gray, A. X. *et al.* Bulk electronic structure of the dilute magnetic semiconductor $Ga_{1-x}Mn_xAs$ through hard x-ray angle-resolved photoemission. *Nat. Mater.* **11**, 957-962 (2012).
[12] Cooper, J. W. Photoelectron-angular-distribution parameters for rare-gas subshells. *Phys. Rev. A* **47**, 1841-1851 (1993).
[13] Yeh, J. J. and Lindau, I. Atomic subshell photoemission cross sections and asymmetry parameters $1 \leq Z \leq 103$. *At. Data Nucl. Data Tables* **32**, 1-155 (1985).
[14] Liang, J. K. *et al.* Crystal structure and superconductivity of $Bi_2Sr_2CaCu_2O_8$ compound. *Mod. Phys. Lett. B* **2**, 483-489 (1988).
[15] Levin, A. A. *et al.* Causes of modulation and hole conductivity of the high-Tc superconductor $Bi_2Sr_2CaCu_2O_{8+\delta}$ according to X-ray single-crystal data, *J. Phys.: Condens. Matter* **6**, 3539-3551 (1994).
[16] He, Y. *et al.* Supermodulation in the atomic structure of the superconductor $Bi_2Sr_2CaCu_2O_{8+\delta}$ from ab initio calculations, *Phys. Rev. B* **77**, 220507 (2008).